



Nanostructured manganese doped ceria solid solutions for CO oxidation at lower temperatures



Perala Venkataswamy, Komateedi N. Rao, Deshetti Jampaiah, Benjaram M. Reddy*

Inorganic and Physical Chemistry Division, CSIR-Indian Institute of Chemical Technology, Uppal Road, Hyderabad 500 007, India

ARTICLE INFO

Article history:

Received 12 April 2014

Received in revised form 20 June 2014

Accepted 21 June 2014

Available online 28 June 2014

Keywords:

CeO₂

Nanostructured Ce_{0.7}Mn_{0.3}O_{2-δ}

Oxygen vacancies

CO oxidation

Synergistic Mn–Ce interaction

ABSTRACT

Noble metal-free nanostructured Ce_{0.7}Mn_{0.3}O_{2-δ} (CM) solid solutions were prepared by a simple, facile, and high yielding coprecipitation method from aqueous solutions of cerium and manganese nitrates. The influence of calcination temperature from 773 to 1073 K on the structural features and catalytic behaviour of the CM solid solutions has been thoroughly investigated. The synthesized materials were characterized using XRD, ICP-OES, BET surface area, TEM and HRTEM, UV–vis DRS, Raman, XPS, EPR, and H₂-TPR techniques. The XRD results indicated that the samples calcined at various temperatures from 773 to 973 K did not show any diffraction peaks corresponding to manganese oxides and thereby ensured the formation of Ce_{0.7}Mn_{0.3}O_{2-δ} solid solution. However, the diffraction peak corresponding to Mn₂O₃ was clearly observed at 1073 K due to the occurrence of phase segregation between Mn–oxide and ceria. The TEM and HRTEM observations showed the nanocrystalline nature of the solid solutions with a particle size in the range of ~7–20 nm. The doping of Mn into the ceria lattice increased the concentration of structural oxygen vacancies, which are beneficial for oxidation reaction as revealed by UV–vis DRS and Raman results. XPS analysis confirmed that Ce and Mn exist in +4 or +3 and +3 or +2 oxidation states, respectively on the surface of the samples. The EPR studies showed the presence of isolated Mn²⁺ and Mn³⁺ species in different structural locations such as ceria-lattice defect sites, framework of Ce⁴⁺ locations, interstitial locations, and at the surface of the ceria. H₂-TPR measurements showed a pronounced enhancement in the reduction of ceria by manganese doping. Among the various catalysts examined, the CM catalyst calcined at 773 K exhibited superior CO oxidation activity at much lower temperature with T₅₀ = 390 K and 100% CO conversion at ~470 K in comparison to pure ceria and MnO_x. The observed remarkable enhancement in the reactivity for CO oxidation at lower temperatures has been attributed to a highly dispersed state of Mn²⁺/Mn³⁺ in the ceria matrix, facile redox behaviour, and a synergistic Mn–Ce interaction.

© 2014 Elsevier B.V. All rights reserved.

1. Introduction

The incessant technological progress and globalization over the past century has rendered a progressive deterioration of natural resources, thereby various hazardous components have been largely emitted into the atmosphere. Among them, carbon monoxide (CO) is the prominent one and it is a trace constituent of the troposphere, produced by both natural processes and human activities [1]. The emission of CO into the atmosphere is mainly due to the incomplete combustion of automobile exhaust engines during the vehicle transportation [2–4]. Apart from this, the CO is also emitted from breathing apparatus, indoor air cleaning, PEM fuel cells, mounting petrochemical industries, closed cycle CO₂ lasers, and

iron smelting [5–7]. Even the presence of a small quantity of CO can show remarkable effect on human health [8]. Therefore, the urgent need to mitigate the harmful impact of CO on the environment is forcing the implementation of catalytic processes to constrain its emission. Until now, various types of heterogeneous catalysts have been prepared and employed for the abatement of CO. Currently, noble metal based catalysts, especially platinum group catalysts represent the state-of-art in internal combustion engine emission technology and have been extensively studied, and resulted a high activity in the oxidation of CO at lower temperatures (<473 K) [4]. However, some of the major problems encountered using these catalysts include high cost, scarcity, sensitivity to sulphur poisoning, and having inferior thermal stability at higher temperatures which prohibit their widespread exploitation in this reaction [8]. Due to these unfavourable reasons, it remains a challenge to find catalysts that can show both good catalytic activity and thermal stability.

* Corresponding author. Tel.: +91 40 27193510; fax: +91 40 2716 0921.

E-mail addresses: bmreddy@iict.res.in, mreddyb@yahoo.com (B.M. Reddy).

It is well known that ceria (CeO_2) has been widely investigated as an important catalytic material over several decades in the field of catalysis such as three-way catalysis, water-gas shift reaction, dehydrogenation reaction, and solid-oxide fuel cells [9,10]. The significance of ceria in pollution abatement and other technologies is mainly due to its distinctive feature of oxygen storage capacity (OSC) associated with the formation of oxygen vacancies and the low redox potential between Ce^{3+} and Ce^{4+} . However, pure CeO_2 is unstable at high temperatures because the progressive agglomeration of its particles results in a decreased OSC and eventual deactivation [11,12]. As a solution, the Ce-based solid solutions formed by doping with other cations into ceria lattice exhibited superior performance due to doping-generated structural defects or newly produced mixed oxide phases [13]. For example, different cations such as cobalt, copper, manganese, chromium, iron, nickel, and vanadium were doped into the ceria and examined for CO oxidation [14]. It has been widely demonstrated that the introduction of lower valent dopant cations could promote the mobility of oxygen ions through the lattice oxide and provide the material with high oxygen ion conductivity, thereby the formation of higher surface and bulk oxygen vacancies to improve the catalyst redox properties of the composite oxides [14–17].

Recently, metal oxides with multiple oxidation states such as manganese oxide have been exploited as suitable materials for catalytic applications due to their high specific capacitance, environmental compatibility, low cost, and non-toxicity [17,18]. Especially in catalysis, the manganese based oxides were used for various catalytic reactions such as combustion of volatile organic compounds, ammonia oxidation, wet oxidation of phenol, and decomposition of NO_x , and the observed superior performances were corroborated to the variable valences of manganese [18]. Due to the possibility of multiple valences for Mn as well as the redox couple associated with Ce, the mixed CeO_2 – MnO_x samples could be intriguing materials for further detailed investigation from both the structural and spectral understanding of the system [17]. For instance, they can be applied as heterogeneous catalysts for the abatement of contaminants in the liquid and gas phases, such as the catalytic reduction of NO and oxidation of acrylic acid and formaldehyde [19], which exhibit much higher catalytic activity than those of pure MnO_x and CeO_2 . Recently, Xingyi et al. [20] described that chlorobenzene can be extensively catalytically combusted by MnO_x – CeO_2 oxides at temperatures as low as 527 K. Delimaris and Ioannides [21] also found that toluene could be oxidized virtually at a temperature of 523 K. Furthermore, CeO_2 – MnO_x was also reported as being extremely active during the low temperature (423 K) selective catalytic reduction (SCR) of NO with NH_3 in the presence of excess oxygen. The observed unique catalytic redox performance of CeO_2 – MnO_x mixed oxide was ascribed to the formation of huge amounts of quite “reactive” surface oxygen species (i.e., O^{2-} , O_2^{2-} , O^- , etc.) on the Mn doped ceria [22]. The present work was undertaken against the aforesaid background. In this work, CeO_2 – MnO_x mixed oxide was synthesized by a facile and most economic coprecipitation method. The optimized Ce/Mn mole ratio was fixed and the effect of calcination temperature on the physicochemical properties and catalytic performance was thoroughly investigated. The techniques of X-ray diffraction (XRD), inductively coupled plasma-optical emission spectroscopy (ICP-OES), Brunauer–Emmett–Teller (BET) surface area, transmission electron microscopy (TEM), high-resolution transmission electron microscopy (HRTEM), UV–vis diffuse reflectance spectroscopy (UV–vis DRS), Raman spectroscopy (RS), X-ray photoelectron spectroscopy (XPS), electron paramagnetic resonance spectroscopy (EPR), and temperature-programmed reduction by hydrogen (H_2 -TPR) were employed to determine the structural/textural properties of the synthesized

catalysts in order to relate these properties with the OSC and CO oxidation activity.

2. Experimental

2.1. Catalyst preparation

An optimized nanocrystalline ceria–manganese (CM, 70:30 mol% based on oxides; $\text{Ce}_{1-x}\text{Mn}_x\text{O}_{2-\delta}$, $x=0.3$) mixed oxide was prepared by a coprecipitation method from ultrahigh dilute aqueous solutions using cerium(III) nitrate ($\text{Ce}(\text{NO}_3)_3 \cdot 6\text{H}_2\text{O}$, Aldrich, AR grade) and manganese(II) nitrate ($\text{Mn}(\text{NO}_3)_2 \cdot 4\text{H}_2\text{O}$, Merck, AR grade) hydrate precursors. The desired amounts of precursors were dissolved separately in double distilled water under mild stirring conditions and mixed together. While stirring this mixture, aqueous ammonia solution was added dropwise into the mixed solution ($\text{pH} \approx 9.5$) so that a brownish colour precipitate was formed, and the stirring was continued constantly for 24 h. Then, the obtained precipitate was filtered off and repeatedly washed with double distilled water until free from anion impurities. The resultant precipitate was oven dried overnight at 373 K and then the dried solid was ground with ceramic mortar. Finally, the well-dispersed powder was calcined for 5 h (the heating and cooling rates were in the steps of 5 K min^{-1}) in a closed electric furnace at 773 K to decompose the residual nitrates to favour the formation of the fluorite phase. Some portions of the calcined powder were again heated for 5 h at 873, 973, and 1073 K, respectively. The synthesized catalysts were designated as CM- T , where T represents the calcination temperature in K. For comparison, pure CeO_2 and MnO_x were also prepared by same method and denoted as C-773 and Mn-773, respectively.

2.2. Catalyst characterization

X-ray powder diffraction patterns were acquired on an X'pert Pro MPD powder diffractometer (PANalytical Company) equipped with a nickel-filtered $\text{Cu K}\alpha$ (0.15418 nm) radiation source and a scintillation counter detector (SCD). The scattered intensity data were collected from 2θ values of 2 – 80° by scanning at 0.01° steps with a counting time of 1 s at each step. Crystalline phases were identified by matching with the International Centre for Diffraction Data Powder Diffraction File (ICDD-PDF). The average crystallite size (D_{XRD}) of the samples was determined with the help of Scherrer equation from line broadening and the lattice parameters were estimated by a standard cubic indexation method using the intensity of the most prominent peak (1 1 1).

The chemical analysis of the prepared samples was performed by inductively coupled plasma optical emission spectroscopy (ICP-OES, Thermo Jarrel Ash model IRIS Intrepid II XDL, USA) to confirm the respective concentrations of elements in the system. For ICP analysis, approximately 50 mg of the sample was dissolved in a solution of 25 mL aqua regia and 475 mL de-ionized water. Then 10 mL of the above solution was diluted to 250 mL.

The surface area and pore size distribution of the as-prepared samples were determined by N_2 adsorption–desorption isotherms at liquid N_2 temperature (77 K) on a Micromeritics (ASAP 2000) analyzer. Specific surface area and pore size distribution were calculated by Brunauer–Emmett–Teller (BET) and Barrett–Joyner–Halenda (BJH) methods, respectively. Prior to the measurements, the samples were pre-treated in a vacuum oven at 473 K for 2 h to remove any residual moisture.

The TEM and HRTEM studies were made on a TECNAIG2 TEM microscope equipped with a slow-scan CCD camera and at an accelerating voltage of 200 kV. The preparation of samples for these

analysis involved sonication in ethanol for 2–5 min and deposition on a copper grid.

UV–vis DRS measurements were performed under ambient conditions using a Varian UV–vis spectrophotometer in the wavelength range of 200–800 nm with an integration sphere diffuse reflectance attachment. The samples under study were diluted with KBr matrix by pelletization.

Raman spectra were recorded at room temperature on a Horiba Jobin-Yvon HR800 Raman spectrometer equipped with a liquid-nitrogen cooled charge coupled device (CCD) detector and a confocal microscope. The line at 632 nm of Ar⁺ ion (Spectra Physics) laser was used as an excitation source for the visible Raman spectroscopy. The laser was focused on the sample under a microscope with the diameter of the analyzed spot being $\sim 1 \mu\text{m}$. The acquisition time was adjusted according to the intensity of Raman scattering. The wavenumber values reported from the spectra are accurate to within 2 cm^{-1} .

The XPS analysis was performed using a PHI 5000 Versa probe (Ulvac-PHI) spectrometer using Mg K α (1253.6 eV) radiation as the excitation source. Analysis was done at room temperature, and the samples were maintained under rigorous vacuum typically in the order of less than 10^{-8} Pa to avoid large amount of noise in the spectra from contaminants. Charging of the catalyst samples was corrected by setting the binding energy of adventitious carbon (C 1s) at 284.5 eV.

The electron paramagnetic resonance measurements were carried out at room temperature with a Bruker EMX spectrometer operating in the X-band. The spectra were calibrated with a standard diphenylpicrylhydrazyl (DPPH) ($g = 2.0036$).

The reducibility of the samples was studied by hydrogen temperature programmed reduction (H_2 -TPR). Approximately 30 mg of the sample mass was placed on top of quartz wool in a U-shaped quartz reactor. The sample was pre-treated at a rate of 10 K min^{-1} to 473 K under a pure He atmosphere at a flow rate of 30 mL min^{-1} for 30 min to clean the surface of the catalysts before TPR investigation. After cooling down to room temperature, the gas atmosphere was switched to 5 vol% H_2/Ar with a rate of 20 mL min^{-1} and the reactor was programmatically heated to 1073 K at 5 K min^{-1} , keeping all the parameters unchanged. Evolving water was removed from the effluent gas by means of a cold molecular sieve trap. A thermal conductivity detector was employed at the outlet of the reactor to measure the volume of hydrogen consumed during the reduction of the samples. All experiments were performed in an automated Micromeritics AutoChem II-2720 instrument.

2.3. Catalytic evaluation

The potential oxygen storage capacity was measured using the oxygen release characteristics of the sample with the help of conventional thermogravimetry (TG) method by employing a commercial Netzsch TG-DTA (Luxx, STA, 409 PC, Germany) analyzer under repeated thermal treatments in the temperature window of 573–1073 K. The weight change of the sample during the thermal treatments was continuously monitored with TG in flowing nitrogen or synthetic air. Approximately 15 mg of ceria-manganese powder was heated in the steps of 5 K min^{-1} up to 1073 K in nitrogen atmosphere (50 mL min^{-1}) in order to release oxygen from the sample. After 10 min of stabilization, synthetic air was introduced resulting to an increase in sample weight due to the uptake of oxygen from air. The observed weight loss during the second stage of thermal treatment is considered as total OSC of the samples represented in $\mu\text{mol O}_2/\text{g catalyst}$.

The activity of the catalysts for the oxidation of CO was measured in the temperature range of 300–773 K at normal atmospheric pressure using a fixed-bed microreactor at a heating ramp of 5 K min^{-1} . The samples (approximately 100 mg, particle size = 250–350 μm)

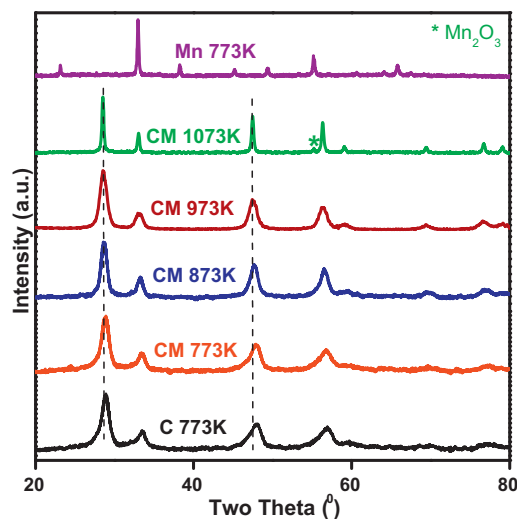


Fig. 1. Powder X-ray diffraction patterns of pure CeO_2 (C) and MnO_x (Mn) calcined at 773 K and $\text{Ce}_{0.7}\text{Mn}_{0.3}\text{O}_{2-\delta}$ (CM) samples calcined at different temperatures from 773 to 1073 K.

were placed in the reactor (2 mm inner diameter and length 250 mm) and diluted with quartz particles with the same particle size, in order to keep a constant volume and better temperature control in the catalytic bed. The reaction temperature was monitored and controlled by using a thermo-couple inserted into the middle of catalyst bed. The following gases and gas mixtures were used (supplied by Air Liquid): argon (>99.999% purity), 9.98% CO (CO purity, >99.997%), and 10.2% O_2 (oxygen purity, >99.995%) with argon as balance. The CO/ O_2 reactant feed ratio was 1, and partial pressures of CO and O_2 were in the range of 10 mbar. The total gas flow rates were guarded by using three mass flow controllers and were in the range of $50\text{--}60 \text{ N mL min}^{-1}$ (millilitres normalized to 273.15 K and 1 atm.). The CO and CO_2 gas concentrations were measured using an Uras 14 infrared analyzer module, and the O_2 concentration was measured using a Magnox 16 analyzer (Hartmann & Braun). Prior to the oxidation of CO, the catalyst was heated to 773 K in a 10.2% O_2/Ar gas mixture, with a heating ramp of 10 K min^{-1} , and kept at the final temperature for 1 h. The oxidized sample was then purged with Argon to avoid gas phase reaction and cooled to the desired starting temperature.

3. Results and discussion

3.1. Characterization studies

The powder XRD patterns of manganese doped ceria catalysts calcined at various temperatures from 773 to 1073 K along with pure CeO_2 and MnO_x calcined at 773 K are shown in Fig. 1. It can be observed that all the diffraction peaks of CM-T ($T = 773, 873$, and 973 K) are characteristic of typical cubic fluorite phase of ceria (JCPDS, No. 34-0394) [23,24]. The absence of diffraction peaks pertaining to manganese oxides, namely, MnO_2 , Mn_2O_3 , and MnO signifies that there are at least two kinds of Mn species present in the samples; (i) Mn ions entered into the ceria lattice and (ii) highly dispersed MnO_x on the surface of ceria [25]. Additionally, it can be noted that the diffraction peaks of these samples are slightly shifted to higher Bragg angles due to incorporation of Mn ions into the ceria lattice. This interesting observation indicates that the doping of Mn^{x+} ($\text{Mn}^{2+} = 0.083 \text{ nm}$; $\text{Mn}^{3+} = 0.065 \text{ nm}$; $\text{Mn}^{4+} = 0.053 \text{ nm}$) ions into the ceria lattice leads to decrease in the lattice parameter due to the smaller size of manganese ions [21]. As shown in Table 1, a decrease of lattice parameter of ceria was evidenced upon doping of manganese ions. These distinct

Table 1

BET surface area (SA), average pore size (nm), pore volume ($\text{cm}^3 \text{g}^{-1}$), average crystallite size (nm), lattice parameter (\AA), and OSC ($\mu\text{mol O}_2/\text{g}$) values of various CM samples calcined at different temperatures from 773 to 1073 K and pure CeO_2 calcined at 773 and 1073 K and MnO_x sample calcined at 773 K.

Sample	SA $\text{m}^2 \text{g}^{-1}$	Average pore size (nm)	Pore volume ($\text{cm}^3 \text{g}^{-1}$)	D (nm)	LP (\AA)	OSC ($\mu\text{mol O}_2/\text{g}$)
Mn 773 K	26	–	–	32.4	4.71	31
C 773 K	41	3.9	0.04	8.92	5.41	40.5
C 1073 K	9.3	17.4	0.03	32.5	5.41	–
CM 773 K	58	30.1	0.44	7.19	5.35	208
CM 873 K	45	32.7	0.37	11.19	5.37	–
CM 973 K	34	36.2	0.31	13.22	5.38	–
CM 1073 K	11	40.6	0.11	22.35	5.41	186

features such as peak shift, difference in the lattice parameters, and absence of diffraction peaks pertaining to MnO_x confirm the formation of Ce–Mn–O solid solutions [26,27]. However, the observed XRD patterns and lattice parameter values of CM-1073 sample are different from other samples and it might be due to the phase separation of ceria–manganese solid solutions, namely, manganese oxides dispersed on cubic ceria phase and a phase of individual Mn_2O_3 appeared at $2\theta = 55.6^\circ$ as shown in Fig. 1 [28]. The above results inferred that the possibility of formation of Ce–Mn–O solid solution can be occurred up to 973 K. These intriguing observations are in well agreement with UV–vis DRS, Raman, and H_2 -TPR studies, which are discussed in the later sections. The average crystallite size (D_{XRD}) of the samples was calculated by means of Scherrer equation and the results are listed in Table 1. The crystallite size of the CM-773 sample was smaller when compared to C-773 and Mn-773, and it might be due to the incorporation of manganese ions into the ceria lattice, thereby inhibition of the crystallite growth [29]. On the other hand, with increasing calcination temperature from 773 to 973 K, the crystallite size was slightly increased from 7.19 to 13.22 nm. A further increase in calcination temperature resulted a drastic enhancement in the crystallite size and reached to 22.35 nm, which is in consistent with the decay in the surface area induced by both sintering and segregation of manganese ions from Ce–Mn–O solid solutions. Moreover, with increase in calcination temperature, an increase in the intensity and decrease in the peak width was observed in the XRD patterns of all CM samples than pure ceria, and such strong and sharp reflections confirmed the growing degree of the crystallinity of the samples. The ICP-OES analysis was further conducted for the elemental analysis of the investigated samples. The molar ratio of Ce and Mn and actual compositions of the investigated materials are summarized in Table S1 (see Supporting Information). It can be concluded that the results are close to the nominal values, which subsequently confirm the stoichiometric concentrations of the single phase materials. As the calcination temperature increases, a slight deviation from the stoichiometry has been found, however the molar ratios of Ce/Mn is close to 7:3.

The porous nature of the prepared CM-*T* ($T = 773, 873, 973$, and 1073 K) samples was evaluated by N_2 -physisorption measurements conducted at 77 K and the corresponding isotherms are compiled in Fig. 2. All the samples showed similar type IV isotherms with clear hysteresis loops located in the relative pressure range of 0.83–0.98, which are associated with the characteristics of mesoporous materials [30]. The BJH pore size distribution (inset) plots of the various CM samples exhibited a superimposition in spite of having minor differences. The different surface characteristics, namely, surface area, pore volume, and pore size of the CM samples at various calcined temperatures in the range of 773–1073 K together with C-773 and C-1073 are summarized in Table 1. It can be noted that the surface area and pore volume of the CM samples are significantly larger than those of C-773 and C-1073 samples, indicating that introduction of Mn ions into the ceria lattice diminished the crystallite size, resulting an increment in the surface area which is in accordance with XRD results [31]. Moreover, as the calcination temperature increased, a systematic decline in both surface area

and pore volume as well as an increase in the value of pore size (30.1–40.6 nm) were observed. Therefore, it is confirmed that the calcination treatment can promote the particle sintering on the surface of the catalyst, thus decreasing the surface area and increasing the pore size. Additionally, the thermal resistance of the CM solid solutions to sintering behaviour is higher when compared to C-773.

The morphology and particle size of the CM-773 and CM-1073 samples could be known by the investigation with transmission electron microscopy and their images are shown in Fig. 3(A) and (B), respectively. It can be seen that the shape of all Ce–Mn–O nanoparticles belongs to hexagonal morphology with nearly monodispersed particles in the range of ~ 7 –20 nm. The HRTEM images (Fig. 3(C) and (D)) of the investigated catalysts clearly display the lattice fringes and it implies that the nanoparticles are well crystallized. For CM-773 sample, the interplanar distance of lattice fringes is 0.309 nm corresponding to (1 1 1) plane of fluorite structured $\text{Ce}_{0.7}\text{Mn}_{0.3}\text{O}_{2-\delta}$ solid solution. On the other hand, for CM-1073 sample, the interplanar distances of lattice fringes are 0.309 and 0.661 nm and can be attributed to (1 1 1) lattice plane of CM-1073 solid solution and (1 1 0) lattice plane of segregated Mn_2O_3 phase, respectively, which is strongly supported by XRD results. The hexagonal morphology of the as-synthesized samples becomes more visible as shown in the insets (Fig. 3(E) and (F)). The absence of lattice fringes related to MnO_x indicates the formation of well-crystallized $\text{Ce}_{0.7}\text{Mn}_{0.3}\text{O}_{2-\delta}$ solid solutions, in which the dopant has entered the lattice and is uniformly distributed throughout it. The average particle sizes of CM-773 and CM-1073 samples were found to be around ~ 7 –10 and 15–20 nm, respectively, which are consistent with the average crystallite sizes obtained from XRD measurements. It can be noted that with increase in calcination temperature, the particle sizes were increased due to the crystallite

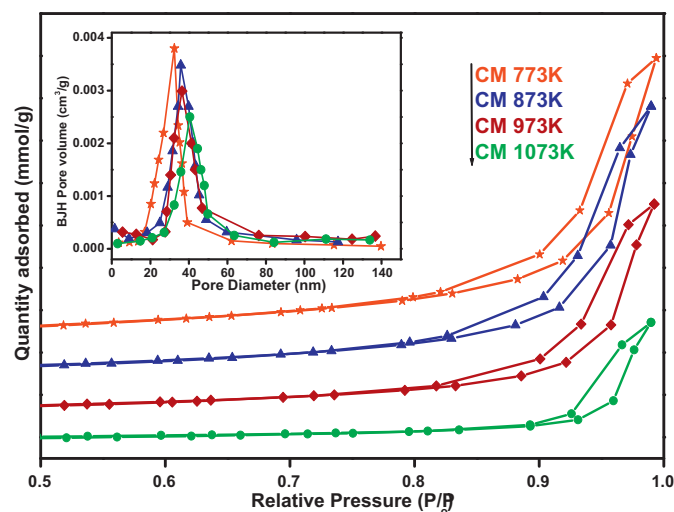


Fig. 2. N_2 adsorption–desorption isotherms of $\text{Ce}_{0.7}\text{Mn}_{0.3}\text{O}_{2-\delta}$ (CM) samples calcined at various temperatures from 773 to 1073 K (inset: pore size distribution curves).

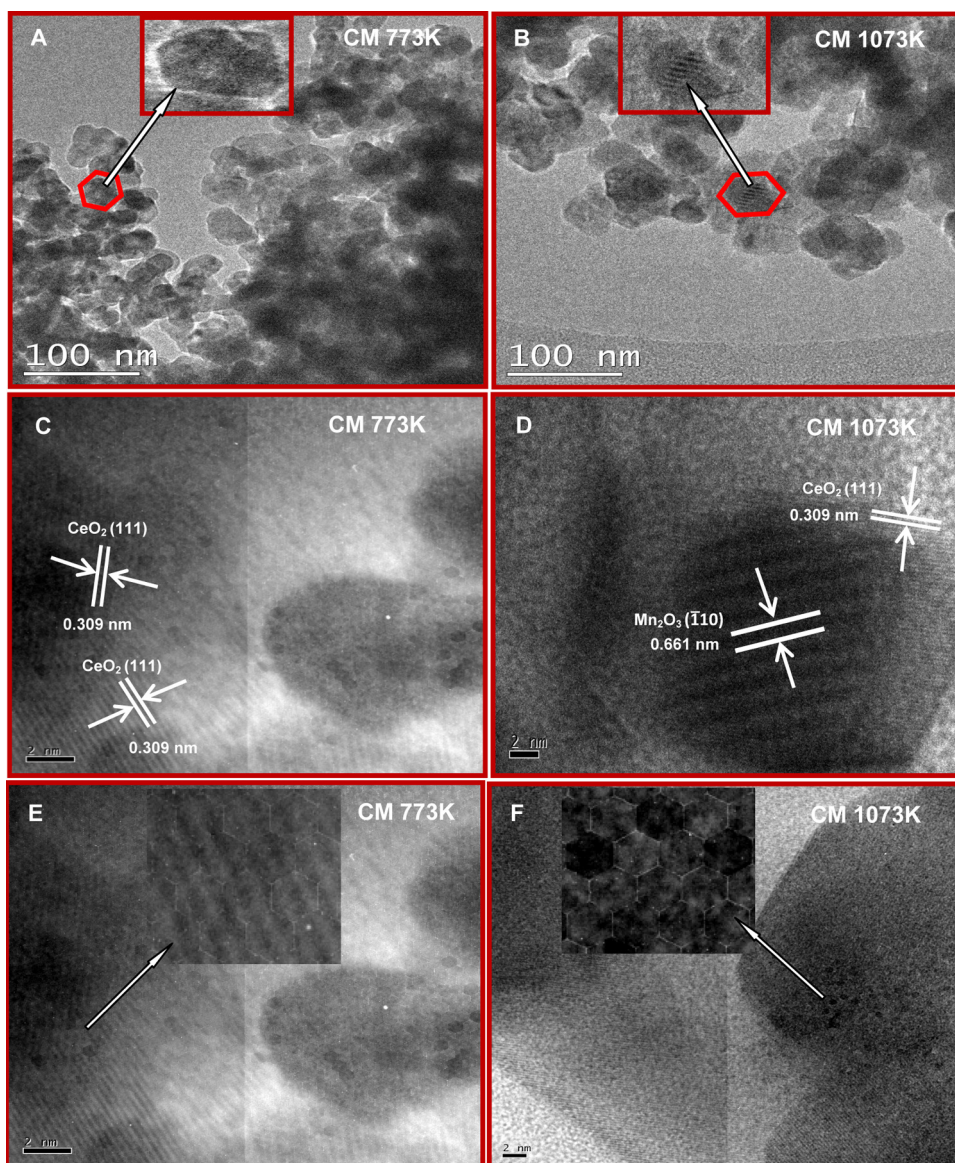


Fig. 3. TEM and HRTEM images of $\text{Ce}_{0.7}\text{Mn}_{0.3}\text{O}_{2-\delta}$ (CM) sample calcined at 773 K (A, C, E) and $\text{Ce}_{0.7}\text{Mn}_{0.3}\text{O}_{2-\delta}$ (CM) sample calcined at 1073 K (B, D, F) (inset: enlarged views of selected areas).

growth and agglomeration of smaller particles at higher temperatures.

UV–vis DRS is a very sensitive probe for identification and characterization of metal ion coordination environment and the existence of oxygen-metal ion charge transfer bands in the nano-sized doped ceria materials, in particular with transition metal oxides [32]. The UV–vis DRS of the C-773 and CM-T ($T=773, 873, 973$, and 1073 K) samples are shown in Fig. 4(A) and (B), respectively. As can be noted from the Fig. 4(A), a split of absorption maxima was observed in the DR spectrum of pure ceria centred at $\sim 253, 287$, and 339 nm corresponding to $\text{O}^{2-} \rightarrow \text{Ce}^{3+}$, $\text{O}^{2-} \rightarrow \text{Ce}^{4+}$ charge-transfer (CT) and inter band transitions (IBT), respectively [33]. In general, the formation of a solid solution not only alters the crystallinity but also affects the charge transfer band positions and optical properties of the catalysts [34]. In the present investigation, DR spectrum of all CM samples displayed well resolved and highly intense absorption bands at ~ 253 and 315 nm. So, the increase of absorption in the UV region (<400 nm) indicates the presence of defects formed in the lattice during the dopant incorporation

[35]. Besides, a partially resolved peak related to IBT was also observed at ~ 397 nm. Compared to C-773, the shifting of the absorption bands ($\text{O}^{2-} \rightarrow \text{Ce}^{4+}$ and IBT) to longer wavelength indicates that the 3d transition metals supply lower unoccupied orbits than Ce 4f, thus the transition from O 2p to the unoccupied orbits requires lower energy [36,37]. Further, the CM samples showed two broad bands in the visible region in addition to the strong absorption in the UV region. The former absorption maxima centred around $580\text{--}585$ nm could be attributed to the ${}^6\text{A}_1 \rightarrow {}^4\text{T}_1$ forbidden d–d transition of Mn^{2+} [38]. The latter absorption band around $735\text{--}740$ nm is related to the characteristic absorption of Mn^{3+} ions, similar to that of pure Mn_2O_3 [38]. It is confirmed that the evidence for the appearance of Mn^{2+} and Mn^{3+} species from DRS study is in concurrence with Raman, XPS, EPR, and TPR results, which are discussed in the following sections. Additionally, the position of the charge transfer bands almost unaffected by thermal treatment indicates the strong interaction between Ce and Mn in the solid solutions. However, for CM-1073 sample, the intensity of the absorption bands was increased and it can be due to the

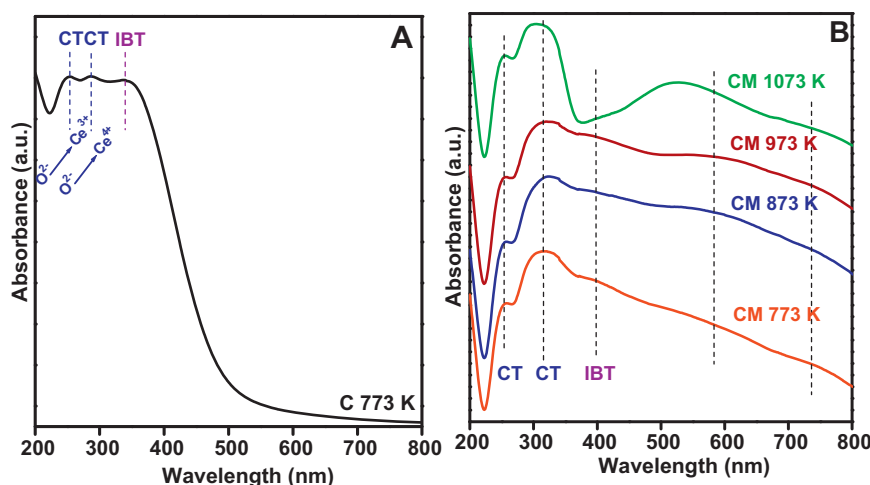


Fig. 4. UV-vis DR spectra of (A) pure CeO_2 (C) calcined at 773 K and (B) $\text{Ce}_{0.7}\text{Mn}_{0.3}\text{O}_{2-\delta}$ (CM) samples calcined at different temperatures from 773 to 1073 K.

crystallite growth with calcination temperature, which is in line with XRD and TEM results. From these studies, it can be noted that the presence of strong absorption bands (UV region) in all CM samples indicates the occurrence of profound oxygen vacancies in the samples. They are very essential for absorption/dissociation of oxygen molecules during the catalytic oxidation reactions, which in turn can affect the catalytic activity of the catalysts [39].

Raman spectroscopy is an intriguing tool to analyze the structural properties of oxide materials particularly nanostructured ceria-based solid solutions. It can provide the fundamental information about the metal-oxygen vibrations found in a lattice and the presence of different crystalline phases which are not observed from XRD studies [40]. Fig. 5 shows the room temperature vis-Raman spectrum of CM-T ($T=773, 873, 973$, and 1073 K) samples along with C-773 and Mn-773. As can be noted from the figure, the spectral pattern of C-773 exhibited a sharp band centred at 465 cm^{-1} , which is corresponding to the triply degenerate F_{2g} active mode and it can be attributed to a symmetrical stretching vibration of the oxygen atoms around cerium cations (Ce^{4+}) in the cubic-phase of CeO_2 [41]. Therefore, the nature and performance

of these vibrational modes are very sensitive to any change in the chemical environment of oxygen sublattice due to induced non-stoichiometry, which is mainly dependent on the nature of the dopant ions [34]. As shown in figure, the visible F_{2g} active mode of all the CM samples is significantly shifted to lower frequency (peak position at $\sim 453\text{--}460\text{ cm}^{-1}$), particularly CM-773 sample with small particle size exhibited large shift with respect to that of C-773 probably due to the formation of Ce-Mn-O solid solution. It can be assumed that changes in the lattice parameter with particle size can affect the Raman peak position [42]. Additionally, the downshift and broadening of the F_{2g} peak can be assigned to the formation of oxygen vacancies, which can also suggest the formation of CM solid solution. This is in good agreement with the results reported by Wu et al. [25]. On the other hand, as the calcination temperature increases, the intensity of the F_{2g} band was increased and become sharper with a shift of its position to 460 cm^{-1} , indicating that Raman shift was less prominent in the case of CM-1073. In addition, a new band with low intensity appeared in all CM samples at $\sim 648\text{--}653\text{ cm}^{-1}$ and it can be assigned to a Mn-O-Mn stretching mode of crystalline Mn_3O_4 phase [43]. Further, the peaks observed at ~ 312 and 369 cm^{-1} (Mn-O-Mn bending modes of Mn_2O_3 and Mn_3O_4) for CM-1073 sample illustrated that the formation of Mn_2O_3 phase at higher calcination temperature and it is also evident by XRD analysis (shown in Fig. 1). Thus, the Raman spectrum fairly confirms the formation of Ce-Mn-O solid solution with the existence of Mn^{2+} and Mn^{3+} ions and this observation could be an interesting complement to EPR technique, which is discussed in the later paragraphs.

The composition and oxidation states of catalyst surface species could be examined by XPS analysis. For this purpose, the XPS spectra of the Ce 3d, Mn 2p and O 1s core levels of CM-773 and CM-1073 samples along with C-773 were recorded and are shown in Figs. 6–8, respectively. The C 1s binding energy value (284.5 eV) was used as a reference to determine the binding energy values of other elements. Fig. 6 depicts the Ce 3d core level XP spectra of CM-773 and CM-1073 along with C-773. Generally, the Ce 3d spectra is known to be complicated due to existence of two different cerium oxidation states and the hybridization of O 2p valence band with the Ce 4f level as well as spin orbit coupling [44]. In order to identify the specific oxidation state of cerium ions i.e., Ce^{4+} and Ce^{3+} , we label the spectra of Ce 3d and shown in Fig. 6. The main features are composed of ten peaks labelled as u and v, which are corresponding to the five pairs of spin-orbit components assigned to $3d_{3/2}$ and $3d_{5/2}$. As can be noted from the figure, the six peaks labelled as u, u'', u''', v, v'', v''' are featured to Ce^{4+} ions, and the

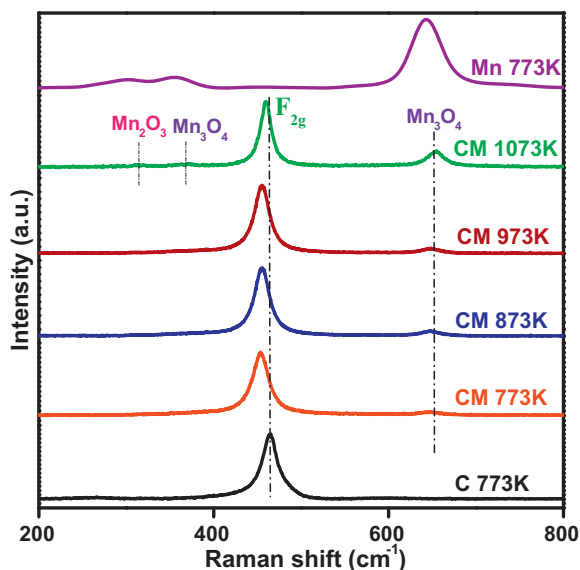


Fig. 5. Raman spectra of pure CeO_2 (C) and MnO_x (Mn) calcined at 773 K and $\text{Ce}_{0.7}\text{Mn}_{0.3}\text{O}_{2-\delta}$ (CM) samples calcined at different temperatures from 773 to 1073 K.

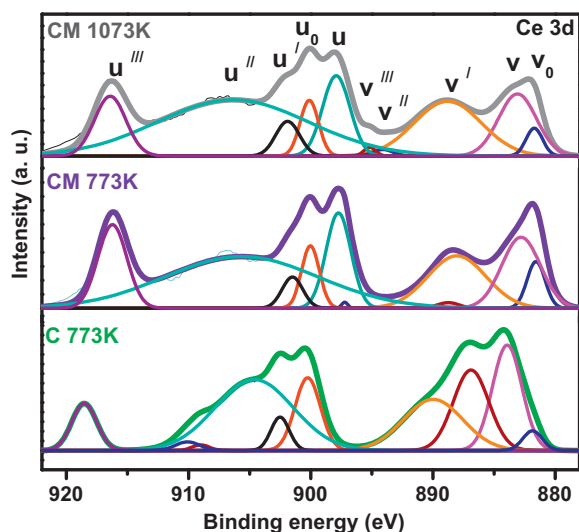


Fig. 6. Ce 3d core level XPS spectra of pure CeO_2 (C) calcined at 773 K and $\text{Ce}_{0.7}\text{Mn}_{0.3}\text{O}_{2-\delta}$ (CM) samples calcined at 773 and 1073 K.

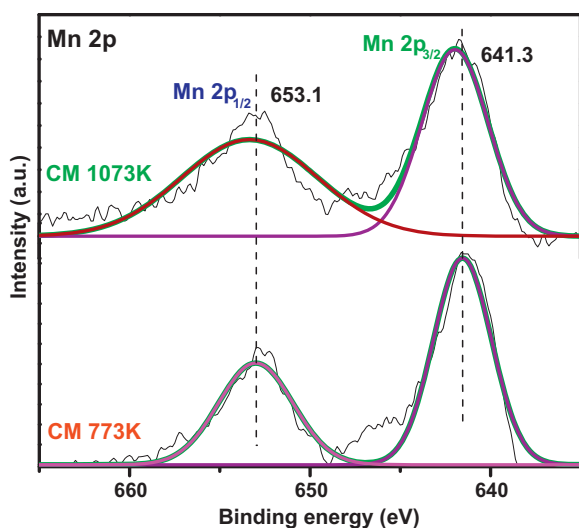


Fig. 7. Mn 2p core level XPS spectra of $\text{Ce}_{0.7}\text{Mn}_{0.3}\text{O}_{2-\delta}$ (CM) samples calcined at 773 and 1073 K.

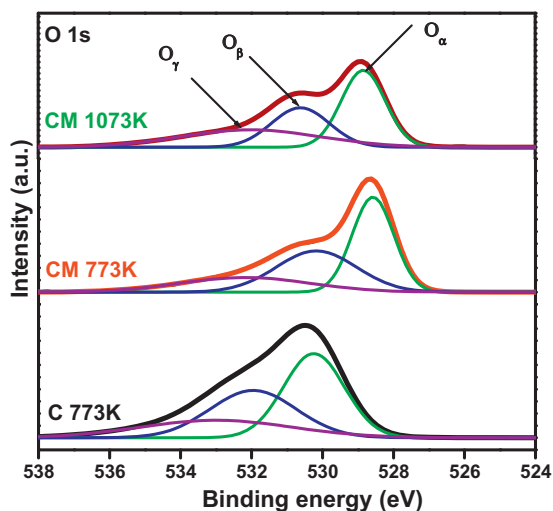


Fig. 8. O 1s core level XPS spectra of pure CeO_2 (C) calcined at 773 K and $\text{Ce}_{0.7}\text{Mn}_{0.3}\text{O}_{2-\delta}$ (CM) samples calcined at 773 and 1073 K.

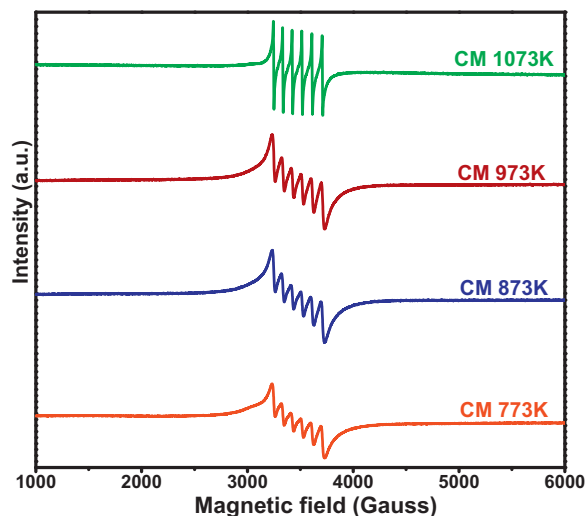
other 4 peaks labelled as u_0 , u' , v_0 , v' are related to Ce^{3+} ions [45]. Among them, the peaks at 882.5, 918.64 and 885.2, 903.7 eV are considered as fingerprints of Ce^{4+} and Ce^{3+} , respectively [46]. The band labelled as u''' in manganese doped ceria samples existed at a lower binding energy compared to pure ceria, indicating that the doping influences the chemical environment of ceria. The shifting of binding energy towards lower side means, the smaller the fraction of Ce^{4+} state and the intensity of the peak often assess the reduction degree of $\text{Ce}^{4+} \rightarrow \text{Ce}^{3+}$ ions in the surface region [47]. Thus, it confirms the coexistence of Ce^{4+} and Ce^{3+} species at the surface. Guan et al. [44] reported that the presence of Ce^{3+} ions could create a charge imbalance, oxygen vacancies, and unsaturated chemical bonds on the catalyst surface. Hence, the migration of oxygen from bulk to surface would become much easier due to formation of Ce^{3+} [44]. Among all samples, the fraction of Ce^{3+} ions order is CM-773 > CM-1073 > C-773. It is well-known that the oxygen vacancies are beneficial for activation of surface oxygen species in CO oxidation reaction. Therefore, it is clear that higher fraction of Ce^{3+} ions in CM-773 sample can act as better catalyst for CO oxidation reaction.

The deconvoluted Mn 2p core level spectra of the CM-773 and CM-1073 samples are shown in Fig. 7. The XP spectrum of Mn 2p exhibited two peaks at 653.1 and 641.3 eV, which can be attributed to Mn 2p_{1/2} and Mn 2p_{3/2} states, respectively. Accordingly, the observed binding energies suggest that Mn is in +2 and +3 oxidation states [48,49]. It is worth noting that the binding energies of the manganese ions in the CM samples are lower than pure MnO and Mn₂O₃ [50], which might be due to a strong interaction between manganese and cerium oxides. Additionally, a distinct identification of the oxidation state (Mn^{2+} and Mn^{3+}) is not possible due to small difference in their binding energies. However, the co-existence of manganese ions in +2 and +3 oxidation states was consistent with the results obtained by XRD, UV–vis DRS, EPR, and H₂-TPR techniques. Moreover, with increasing calcination temperature, a small decrease in the intensity of the peak maxima of Mn 2p_{1/2} and Mn 2p_{3/2} was observed.

The O 1s core level spectra of CM-773, CM-1073 samples and C-773 are illustrated in Fig. 8. It can be observed from the figure that the O 1s spectrum is broad and complicated due to the presence of more than one peak arising from the overlapping contributions of different chemical oxygen species bounded to Ce and Mn in the samples. In order to differentiate these oxygen species, the spectra was resolved with Gaussian-Lorentz model functions and the curve fitted into three peaks. The peaks observed for C-773 at 530.2, 531.9, and 533.5 eV can be attributed to lattice oxygen atoms associated with the oxide (O_α), surface adsorbed oxygen (O_β), and chemisorbed water and/or carbonates (O_γ), respectively [51]. The binding energy of most intense peak (O_α) in pure ceria shifted to lower binding energy side in CM-773 (528.5 eV) and CM-1073 (528.8 eV) samples, indicating that a change in structural arrangement and/or electronic structure alteration due to synergistic interaction between Ce–O and Mn–O. Additionally, in order to know the influence of various atomic oxygen species, the surface atomic concentration was calculated by integrating peak areas of the O 1s spectra and the values are shown in Table 2. The binding energies of surface adsorbed oxygen (O_β) for C-773, CM-773, and CM-1073 are 531.9, 530.2, and 530.5 eV, respectively. Due to the existence of Ce^{3+} ions, the oxygen vacancies can be created on the catalyst surface [44]. Thus, the enhancement of Ce^{3+} concentration is helpful for an increase in surface adsorbed oxygen on the surface. As observed from Table 2, the CM-773 catalyst contained the highest relative surface atomic concentration (36.11%) of O_β species. It is well acknowledged in the literature that the surface adsorbed oxygen atoms (O_β) are vital in most of the catalytic oxidation reactions [45,52]. Therefore, it can be evidenced that the “ O_β ” is the significant active oxygen species and it can be responsible for the high catalytic activity of CM-773 for the oxidation of CO. With

Table 2Binding energies and surface atomic concentrations of pure CeO₂ calcined at 773 K and CM samples calcined at 773 and 1073 K.

Sample	Ce 3d (u ^{'''}) (eV)	O 1s centre (eV)			Surface atomic concentration O/O _T (%)		
		O _α	O _β	O _γ	O _α	O _β	O _γ
C 773 K	918.64	530.2	531.9	533.5	43.25	34.44	22.31
CM 773 K	916.34	528.5	530.2	532.4	43.05	36.11	20.84
CM 1073 K	916.45	528.8	530.5	531.9	41.82	28.27	29.91

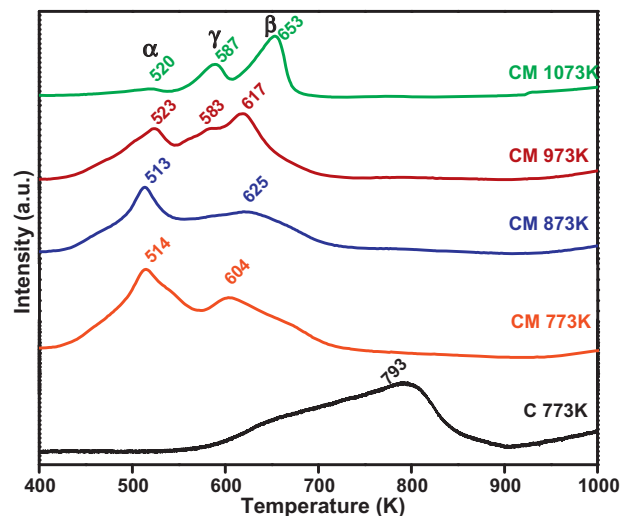
O_α, lattice oxygen; O_β, surface adsorbed oxygen; O_γ, chemisorbed water and/or carbonates.**Fig. 9.** Electron paramagnetic resonance spectra of Ce_{0.7}Mn_{0.3}O_{2-δ} (CM) samples calcined at different temperatures from 773 to 1073 K.

increase in calcination temperature, the three distinguished peaks (O_α, O_β, O_γ) in CM-1073 are slightly shifted to higher binding energy side and the intensity of the peaks are decreased. The observed phenomena ensured that the environment of oxygen species was changed owing to thermal treatment.

To identify possible oxidation states and coordination environment of Mn species in Mn doped ceria calcined at various temperatures in the range of 773–1073 K were investigated by EPR spectroscopy. The powdered X-band (9.8 GHz) EPR spectra of all CM samples measured at room temperature are shown in Fig. 9 and the corresponding EPR parameters are summarized in Table 3. The spectra are well-resolved and all samples exhibited an intense six hyperfine lines centred at $g = 2.0043$ with the average hyperfine coupling constant “A” of approximately 92 G. From several reports, it can be confirmed that the observed g and A values are attributed to typical Mn²⁺ ions [49,53,54]. These isolated Mn²⁺ ions might be concentrated somewhere in the solid solutions probably at defect sites with a non-cubic symmetry in framework of Ce⁴⁺ sites and surface of the samples [54]. Additionally, it is well-known that Mn⁴⁺ can also render similar type of EPR spectra, but virtually it shows signals below free spin “ g ” factor at 1.96 with hyperfine coupling constant of “A” at 76 G [49]. Therefore, the present EPR spectra fairly confirmed the absence of Mn⁴⁺ ions irrespective of calcination temperatures. Moreover, with increasing calcination

Table 3 g factor and hyperfine values “A” of various CM samples calcined at different temperatures from 773 to 1073 K.

Sample	g Factor	A (G)
CM 773 K	2.000	92.5
CM 873 K	2.003	92.3
CM 973 K	2.007	92.1
CM 1073 K	2.009	91.7

**Fig. 10.** H₂ consumption as a function of temperature for Ce_{0.7}Mn_{0.3}O_{2-δ} (CM) samples calcined at different temperatures from 773 to 1073 K and along with pure CeO₂ (C) calcined at 773 K.

temperature from 773 to 1073 K, the EPR patterns did not show much difference in their “ g ” and “A” values, but the intensities of signals significantly enhanced and become narrower. The observed enhancement in EPR signals probably owing to an increase in the concentration of Mn²⁺ ions [55]. In addition to +2 and +4 oxidation states, Mn can also exhibit +3 oxidation state. Unfortunately, Mn³⁺ ions would not contribute to EPR due to its large zero field splitting and they can be detected only at very low temperatures with high frequency (e.g. W-band). However, Jia et al. [54] reported that the Mn can exhibit +3 oxidation state in MnCe and MnCeZr samples. According to them, the increased intensity of EPR signals can be due to the presence of some Mn³⁺ ions and thereafter converted to Mn²⁺ ions which are detected by EPR spectroscopy. Therefore, our EPR results confirmed that the Mn was in +2 and +3 oxidation states and it was consistent with UV–vis DRS, Raman, and XPS results.

The H₂-TPR profiles of Mn doped ceria catalysts calcined at various temperatures in the range of 773–1073 K along with C-773 are shown in Fig. 10. Generally, pure ceria exhibits two reduction peaks pertaining to the surface and bulk reduction which are centred at ~793 and 1100 K (not shown), respectively [41]. The difference in these two successive reduction temperatures is due to the different binding energy of oxygen to cerium cations in the lattice [56]. However, the reduction patterns were different when Mn was doped into the ceria lattice, and they precisely indicated that the surface and bulk reduction temperatures of pristine ceria were reduced to lower temperatures. As can be noted from the figure, the TPR plots of the CM catalysts calcined at 773 and 873 K clearly showed two reduction peaks and they were designated as α and β in the figure. The former peak (α) was located at ~514 K for both the samples, whereas the latter peak (β) was observed at ~604 and ~625 K for CM-773 and CM-873 samples, respectively. To assess these reduction peaks, we have provided the H₂-TPR pattern of pure MnO_x calcined at 773 K (see Fig. S1 in supporting information).

Accordingly, the low temperature peak (α) could be attributed to the readily reducible and highly dispersed surface manganese species with the reduction of $\text{MnO}_2/\text{Mn}_2\text{O}_3$ to Mn_3O_4 and the high temperature reduction peak (β) was assigned to the reduction of Mn_3O_4 to MnO together with the reduction of surface ceria [57]. The CM-973 and CM-1073 catalysts also showed α peak at ~ 523 K, but the β peak is located at 617 and 653 K, respectively. Based on these observations, it can be concluded that the low temperature reduction patterns can be attributed to the synergistic interaction between Mn–O and Ce–O with the formation of a $\text{Ce}_{0.7}\text{Mn}_{0.3}\text{O}_{2-\delta}$ solid solution, in which the mobility of oxygen species from bulk to the surface was greatly enhanced thereby creating more active sites on the surface for the adsorption of hydrogen [58]. Interestingly, extra peaks were observed at ~ 583 and 587 K for the CM-973 and CM-1073 catalysts, respectively, which can be attributed to the Mn_2O_3 phase (designated as γ). This observation indicates that Mn_2O_3 phase is segregated from the $\text{Ce}_{0.7}\text{Mn}_{0.3}\text{O}_{2-\delta}$ solid solution at high calcination temperature. Furthermore, with increasing the calcination temperature, the peaks were shifted to higher temperatures and also the intensity of “ α ” peak in each TPR profile of CM samples was decreased as well as “ β ” peak intensity was increased. It can be noted that the discrepancy of the intensities of the above peaks might be due to the decrease in the synergetic interaction between the manganese and ceria species which is fairly evidenced by XRD, Raman, and UV–vis DRS studies.

3.2. Activity studies

The OSC mainly relies on transport properties such as oxygen diffusion at the surface or in the bulk of oxides, which are prominent to catalyze oxidation reactions, particularly in CO oxidation [59]. The OSC of C-773, Mn-773, CM-773 and CM-1073, which was measured by thermogravimetry method, were presented in Table 1. Among all samples, the CM-773 sample exhibited the highest OSC value ($208 \mu\text{mol O}_2/\text{g}$). Generally, the oxygen vacancies in pure ceria are originated due to its redox property [60]. Interestingly, in the case of CM-773, the oxygen vacancies are created not only due to the conversion of Ce^{4+} to Ce^{3+} but also the substitution of $\text{Mn}^{2+/3+}$ ions into ceria lattice [19]. As a result, the mobility and amount of oxygen vacancies both in the bulk as well as on the surface are increased, which leads to enhancement of OSC. Furthermore, the observed superior OSC of CM-773 sample was supported by the results from UV–vis DRS and Raman studies as discussed earlier. However, with increase in calcination temperature, the lowering of OSC value of CM-1073 was owing to loss of specific surface area because of growth of the crystallite sizes and segregation of the manganese oxide phase from the solid solution as observed from XRD and TEM results.

The profiles for CO conversion as a function of reaction temperature over CeO_2 – MnO_x mixed oxides calcined at 773 and 1073 K along with C-773 and Mn-773 were presented in Fig. 11. Xu et al. [61,62] suggested that the catalytic oxidation of CO over metal oxides could proceed in two different pathways, namely, Mars–van Krevelen and Langmuir–Hinshelwood mechanism. Accordingly, the former mechanism can be predominant at temperatures higher than 463 K, where adsorbed CO (CO_{ad}) is mainly oxidized by lattice oxygen ($\text{O}_{\text{lattice}}$). On the other hand, in the latter case the CO_{ad} is oxidized mainly by adsorbed oxygen (O_{ad}) in the temperature below 463 K. Therefore, the mobility and/or reducibility of the active oxygen (O_{ad} and/or $\text{O}_{\text{lattice}}$) is of crucial importance for CO oxidation reaction. As explained earlier from XPS, superoxide species or lattice oxygen atoms formed on Ce–Mn–O solid solution associated with both the redox couples ($\text{Mn}^{2+}/\text{Mn}^{3+}$ or $\text{Ce}^{3+}/\text{Ce}^{4+}$) directly participate in CO oxidation. Therefore, the introduction of lower valent with multiple oxidation states of Mn dopant could enhance the reactivity of ceria by modifying

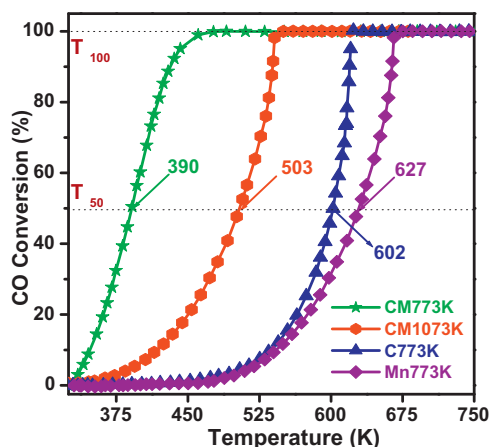


Fig. 11. Conversion of CO (%) versus Temperature (K) for pure CeO_2 (C) and MnO_x (Mn) calcined at 773 K and $\text{Ce}_{0.7}\text{Mn}_{0.3}\text{O}_{2-\delta}$ (CM) sample calcined at 773 and 1073 K.

the rate of vacancy exchange between the bulk and the oxide surface, and by facilitating the migration of oxygen vacancies from the bulk to the oxide surface [17,19]. Considering the above analysis, it is evident from the figure that both CM samples were found to be catalytically more active for the conversion of CO to CO_2 while compared to C-773 and Mn-773. The light-off temperatures of the investigated CM samples were noticed at ~ 390 and 503 K, respectively, where C-773 and Mn-773 showed at ~ 602 and 627 K. Among all the samples, CM-773 exhibited extremely low T_{50} (temperature at which the 50% CO conversion is achieved) and remaining samples were shown greater T_{50} irrespective of 100% CO conversion at around ~ 470 K. As discussed earlier, the CM-773 catalyst might follow the Langmuir–Hinshelwood mechanism. In contrast, as the temperature increases, the lattice oxygen of CM-1073 catalyst is considered to be the primary active species for oxidizing CO following the Mars–van Krevelen mechanism. Overall, the sequence of catalytic activity expressed as CO conversion is CM-773 > CM-1073 > C-773 > Mn-773. Additionally, we plotted the light-off curves based on surface area for all the investigated catalysts as a function of reaction temperature and shown in Fig. S2. As observed from the figure, the Mn doped ceria sample calcined at 773 K exhibits higher surface area as well as superior activity compared to all other catalysts. Therefore, it is clear that the large difference in the light-off temperatures of CM-773, C-773 and Mn-773 could be due to the synergetic interaction of Ce and Mn species as well as owing to the following properties: (i) the higher specific surface area and smaller particle size of the CM-773 sample, (ii) the abundant number of surface/bulk oxygen vacancies, which is confirmed from UV–vis DRS, Raman, and XPS studies, and (iii) the surface redox properties exhibited by the CM-773 sample as observed from TPR. Furthermore, the activity of the samples can be directly correlated with the OSC values (Table 1), which demonstrated that the sample with higher OSC confers superior activity for CO oxidation. Accordingly, the CM-773 has shown higher OSC value than C-773 and Mn-773. The above mentioned all characteristics of CM-773 sample are responsible for the enhancement of low temperature activity of CO oxidation. Further, the relationship between the catalytic activity of CO oxidation and textural properties of the probed samples are plotted in Fig. 12. The CM-1073 sample exhibited inferior activity ($T_{50} = \sim 503$ K) compared to the CM-773 sample, which can be primarily due to the less surface area, low OSC and decrease in synergetic interaction of Mn and ceria because of segregation of Mn_2O_3 phase from the solid solution. Interestingly, the CM-1073 sample exhibited a plausibly better activity than that of C-773 and Mn-773, we believe that, it might be due to the presence of segregated Mn_2O_3 phase, which itself

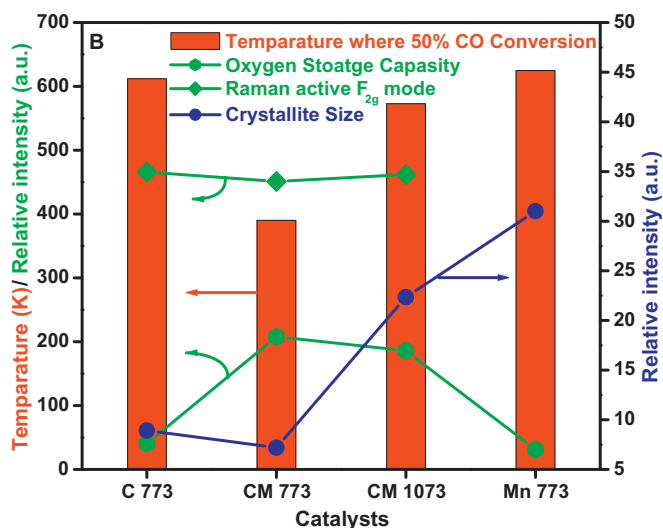


Fig. 12. The relationship between the catalytic activities of CO oxidation (K) and textural/reducible properties of pure CeO₂ (C) and MnO_x (Mn) calcined at 773 K and Ce_{0.7}Mn_{0.3}O_{2-δ} (CM) sample calcined at 773 and 1073 K.

acts as oxidation catalyst and responsible for high CO conversion. Combined with all the above scenario, the CM-773 was confirmed as a suitable catalyst for low temperature CO oxidation.

4. Conclusions

In summary, we have prepared nanocrystalline Mn doped ceria solid solutions with high surface area by a co-precipitation method and their catalytic properties were studied by various physicochemical techniques towards CO oxidation. The investigated catalysts showed the excellent low temperature CO oxidation performance while compared to pure ceria. Particularly, the CM-773 catalyst exhibited the superior CO activity in terms of light-off temperature ($T_{50} = 390$ K) and it could be mostly attributed to the high surface area, reducibility, more surface oxygen defects and a high OSC at low temperatures. These intriguing observations are mainly due to the strong synergistic effect between MnO_x and CeO₂ species and the improvement in redox properties of ceria, thus facilitating the formation of surface oxygen vacancies leading to the availability of active oxygen for CO oxidation at relatively low temperatures (~390 K). Moreover, the facile redox behaviour of Mn²⁺/Mn³⁺ in the ceria matrix is a fascinating property that can be exploited in the oxidation–reduction reactions such as oxygen storage and release modes, which could be further utilized for CO oxidation. The high catalytic activity revealed by the present CM catalysts for low temperature CO oxidation reaction is hopeful and could be substitute for highly expensive noble metal catalysts.

Supporting information

Detailed information about the chemical composition of Ce_{0.7}Mn_{0.3}O_{2-δ} catalysts calcined at various temperatures are summarized in Table S1, H₂-TPR pattern of pure MnO_x catalyst calcined at 773 K in Figure S1 and light-off curve based on BET surface area of investigated catalysts calcined at various temperatures in Figure S2.

Acknowledgements

We greatly acknowledge Prof. Dr. W. Grünert, Ruhr University Bochum, Germany for providing CO oxidation results. PV thanks Council of Scientific and Industrial Research (CSIR), New Delhi for

the Senior Research Fellowship. DJ thanks IICT-RMIT Joint Research Centre for the award of Junior Research Fellowship. Financial support was received from the Department of Science and Technology, New Delhi, under SERB Scheme (SB/S1/PC-106/2012).

Appendix A. Supplementary data

Supplementary data associated with this article can be found, in the online version, at <http://dx.doi.org/10.1016/j.apcatb.2014.06.038>.

References

- [1] A. Trovarelli, P. Fornasiero, Catalysis by Ceria and Related Materials, in: Catalytic Science Series, vol. 12, Imperial College Press, UK, 2013.
- [2] F. Yang, J. Graciani, J. Evans, P. Liu, J. Hrbek, J.F. Sanz, J.A. Rodriguez, J. Am. Chem. Soc. 133 (2011) 3444–3451.
- [3] P. Larsson, A. Andersson, J. Catal. 179 (1998) 72–89.
- [4] B.M. Reddy, K.N. Rao, P. Bharali, Ind. Eng. Chem. Res. 48 (2009) 8466–8478.
- [5] L.-H. Chang, N. Sasirekha, B. Rajesh, Y.-W. Chen, Sep. Purif. Technol. 58 (2007) 211–218.
- [6] H.-J. Freund, G. Meijer, M. Scheffler, R. Schlögl, M. Wolf, Angew. Chem. Int. Ed. 50 (2011) 10064–10094.
- [7] H. Zhu, Z. Qin, W. Shan, W. Shen, J. Wang, J. Catal. 233 (2005) 41–50.
- [8] N. Imanaka, T. Masui, H. Imadzu, K. Yasuda, Chem. Commun. 47 (2011) 11032–11034.
- [9] P.R.L. Keating, D.O. Scanlon, G.W. Watson, J. Mater. Chem. C 1 (2013) 1093–1098.
- [10] V.M. Shinde, G. Madras, Appl. Catal. B 138–139 (2013) 51–61.
- [11] D. Stošić, S. Bennici, V. Rakić, A. Auroux, Catal. Today 192 (2012) 160–168.
- [12] B.M. Reddy, G. Thirumurthulu, L. Katta, J. Phys. Chem. C 113 (2009) 15882–15890.
- [13] S. Collins, G. Finos, R. Alcántara, E. del Rio, S. Bernal, A. Bonivardi, Appl. Catal. A 388 (2010) 202–210.
- [14] S.-L. Zhong, L.-F. Zhang, L. Wang, W.-X. Huang, C.-M. Fan, A.-W. Xu, J. Phys. Chem. C 116 (2012) 13127–13132.
- [15] T. Li, G. Xiang, J. Zhuang, X. Wang, Chem. Commun. 47 (2011) 6060–6062.
- [16] X. Yao, C. Tang, Z. Ji, Y. Dai, Y. Cao, F. Gao, L. Dong, Y. Chen, Catal. Sci. Technol. 3 (2013) 688–698.
- [17] B. Murugan, A.V. Ramaswamy, Chem. Mater. 7 (2005) 3983–3993.
- [18] Z. Chen, Z. Jiao, D. Pan, Z. Li, M. Wu, C.-H. Shek, C.M.L. Wu, J.K.L. Lai, Chem. Rev. 112 (2012) 3833–3855.
- [19] Z. Wang, G. Shen, J. Li, H. Liu, Q. Wang, Y. Chen, Appl. Catal. B 138–139 (2013) 253–259.
- [20] W. Xingyi, K. Qian, L. Dao, Appl. Catal. B 86 (2009) 166–175.
- [21] D. Delimaris, T. Ioannides, Appl. Catal. B 84 (2008) 303–312.
- [22] W. Cen, Y. Liu, Z. Wu, H. Wang, X. Weng, Phys. Chem. Chem. Phys. 14 (2012) 5769–5777.
- [23] W.-J. Hong, S. Iwamoto, S. Hosokawa, K. Wada, H. Kanai, M. Inoue, J. Catal. 277 (2011) 208–216.
- [24] P. Sudarshanam, B. Mallesham, P.S. Reddy, D. Großmann, W. Grünert, B.M. Reddy, Appl. Catal. B 144 (2014) 900–908.
- [25] X. Wu, S. Liu, D. Weng, F. Lin, R. Ran, J. Hazard. Mater. 187 (2011) 283–290.
- [26] M. Machida, M. Uto, D. Kurogi, T. Kijima, Chem. Mater. 12 (2000) 3158–3164.
- [27] T. Akashi, S. Sato, R. Takahashi, T. Sodesawa, K. Inui, Catal. Commun. 4 (2003) 411–416.
- [28] A. Bensalem, F. Bozon-Verduraz, M. Delamar, G. Bugli, Appl. Catal. A 121 (1995) 81–93.
- [29] X. Tang, J. Chen, Y. Li, Y. Li, Y. Xu, W. Shen, Chem. Eng. J. 118 (2006) 119–125.
- [30] Z.-Q. Zou, M. Meng, Y.-Q. Zha, J. Phys. Chem. C 114 (2009) 468–477.
- [31] L. Xuesong, L. Jiqing, Q. Kun, H. Weixin, L. Mengfei, J. Rare Earths 27 (2009) 418–424.
- [32] M. Raciulete, P. Afanasiev, Appl. Catal. A 368 (2009) 79–86.
- [33] K.N. Rao, P. Bharali, G. Thirumurthulu, B.M. Reddy, Catal. Commun. 11 (2010) 863–866.
- [34] D.H. Prasad, S.Y. Park, H.-I. Ji, H.-R. Kim, J.-W. Son, B.-K. Kim, H.-W. Lee, J.-H. Lee, J. Phys. Chem. C 116 (2012) 3467–3476.
- [35] G.R. Rao, H.R. Sahu, Proc. Indian Acad. Sci. 113 (2001) 651–658.
- [36] L. Yue, X.-M. Zhang, J. Alloys Compd. 475 (2009) 702–705.
- [37] C. Xia, C. Hu, P. Chen, B. Wan, X. He, Y. Tian, Mater. Res. Bull. 45 (2010) 794–798.
- [38] F. Milella, J.M. Gallardo-Amores, M. Baldi, G. Busca, J. Mater. Chem. 8 (1998) 2525–2531.
- [39] M. Guo, J. Lu, Y. Wu, Y. Wang, M. Luo, Langmuir 27 (2011) 3872–3877.
- [40] H. Knozinger, G. Mestl, Top. Catal. 8 (1999) 45–55.
- [41] B.M. Reddy, L. Katta, G. Thirumurthulu, Chem. Mater. 22 (2010) 467–475.
- [42] J.E. Spanier, R.D. Robinson, F. Zhang, S.-W. Chan, I.P. Herman, Phys. Rev. B 64 (2001) 245407–245415.
- [43] B. Fazio, L. Spadaro, G. Trunfio, J. Negro, F. Arena, J. Raman Spectrosc. 42 (2011) 1583–1588.
- [44] B. Guan, H. Lin, L. Zhu, Z. Huang, J. Phys. Chem. C 115 (2011) 12850–12863.
- [45] F. Larachi, J. Pierre, A. Adnot, A. Bernis, Appl. Surf. Sci. 195 (2002) 236–250.
- [46] K.N. Rao, P. Venkataswamy, B.M. Reddy, Ind. Eng. Chem. Res. 50 (2011) 11960–11969.

- [47] M. Yan, T. Mori, J. Zou, F. Ye, D.R. Ou, J. Drennan, *Acta Mater.* 57 (2009) 722–731.
- [48] G. Blanco, M.A. Cauqui, J.J. Delgado, A. Galtayries, J.A. Perez-Omil, J.M. Rodriguez-Izquierdo, *Surf. Interface Anal.* 36 (2004) 752–755.
- [49] B. Murugan, A.V. Ramaswamy, *J. Phys. Chem. C* 112 (2008) 20429–20442.
- [50] L. Liu, Q. Yu, J. Zhu, H. Wan, K. Sun, B. Liu, H. Zhu, F. Gao, L. Dong, Y. Chen, *J. Colloid Interface Sci.* 349 (2010) 246–255.
- [51] C. Zhang, C. Wang, W. Zhan, Y. Guo, Y. Guo, G. Lu, A. Baylet, A. Giroir-Fendler, *Appl. Catal. B* 129 (2013) 509–516.
- [52] H. Li, C.-Y. Wu, Y. Li, J. Zhang, *Environ. Sci. Technol.* 45 (2011) 7394–7400.
- [53] G.S. Kumar, M. Palanichamy, M. Hartmann, V. Murugesan, *Microporous Mesoporous Mater.* 112 (2008) 53–60.
- [54] L. Jia, M. Shen, J. Hao, T. Rao, J. Wang, *J. Alloys Compd.* 454 (2008) 321–326.
- [55] G. Qi, R.T. Yang, *J. Phys. Chem. B* 108 (2004) 15738–15747.
- [56] N. Sutradhar, A. Sinhamahapatra, S. Pahari, M. Jayachandran, B. Subramanian, H.C. Bajaj, A.B. Panda, *J. Phys. Chem. C* 115 (2011) 7628–7637.
- [57] X. Wu, Q. Liang, D. Weng, J. Fan, R. Ran, *Catal. Today* 126 (2007) 430–435.
- [58] X. Tang, Y. Li, X. Huang, Y. Xu, H. Zhu, J. Wang, W. Shen, *Appl. Catal. B* 62 (2006) 265–273.
- [59] K. Ahn, D.S. Yoo, D.H. Prasad, H.-W. Lee, Y.-C. Chung, J.-H. Lee, *Chem. Mater.* 24 (2012) 4261–4267.
- [60] K. Kuntaiah, P. Sudarsanam, B.M. Reddy, A. Vinu, *RSC Adv.* 3 (2013) 7953–7962.
- [61] J. Xu, Y.-Q. Deng, Y. Luo, W. Mao, X.-J. Yang, Y.-F. Han, *J. Catal.* 300 (2013) 225–234.
- [62] J. Xu, P. Li, X. Song, C. He, J. Yu, Y.-F. Han, *J. Phys. Chem. Lett.* 1 (2010) 1648–1654.